Multisource statistically optimized near-field acoustical holography

Alan T. Wall,[a] Kent L. Gee, and Tracianne B. Neilsen
N243 Eyring Science Center, Brigham Young University, Provo, Utah 84602

(Received 10 July 2014; revised 31 December 2014; accepted 13 January 2015)

This paper presents a reduced-order approach to near-field acoustical holography (NAH) that allows the user to account for sound fields generated by multiple spatially separated sources. In this method, an equivalent wave model (EWM) of a given field is formulated to include combinations of planar, cylindrical, spherical, or other elementary wave functions in contrast to an EWM restricted to a single separable coordinate system. This can alleviate the need for higher-order functions, reduce the number of measurements, and decrease error. The statistically optimized near-field acoustical holography (SONAH) algorithm is utilized to perform the NAH projection after the formulation of the multisource EWM. The combined process is called multisource statistically optimized near-field acoustical holography (M-SONAH). This method is used to reconstruct simulated sound fields generated by combinations of a vibrating piston in a sphere and linear arrays of monopole sources. It is shown that M-SONAH can reconstruct near-field pressures in multisource environments with lower errors and fewer measurements than a strictly plane or cylindrical-wave formulation using the same simulated measurement. © *2015 Acoustical Society of America*.

[http://dx.doi.org/10.1121/1.4906585]

[EGW] Pages: 963–975

I. INTRODUCTION

The identification of noise sources from a radiating object is a critical first step for the design strategy of noise reduction measures. The current paper presents an approach to near-field acoustical holography (NAH) for the modeling of sound fields generated by multiple spatially distinct sources. It is based on the formulation of an equivalent wave model (EWM) that is not restricted to functions from a single orthogonal basis, but rather allows combinations of multiple types of wave functions with varied origins. Such an EWM can reduce the need for high-order terms to represent the total field. Reduced-order terms make the matrix solution less susceptible to noise contamination, which simplifies regularization and makes reconstructions more robust. Since lower-order terms require less-dense measurements, another benefit of multisource EWM modeling is a reduction in the number of required hologram measurement points.

In order to discuss the application of NAH to multisource configurations, it is helpful to consider how NAH and other imaging techniques—directly or implicitly—all represent sound fields with an EWM. An EWM is typically a linear combination of spatial basis functions, or elementary wave functions. [Note that many authors also discuss the idea of an equivalent source model, or ESM (e.g., Semenova and Wu, 2005; Tam *et al*., 2010; Morgan *et al*., 2012). Because of the similarities, the current methods could also be applied to ESM methods, since both represent sound fields with analytical wave functions.] In any acoustical imaging method, the EWM consists of wave functions that must obey the homogeneous wave equation or, in the frequency domain, the Helmholtz equation. Thus, the superposition of these waves represents a total field that also obeys the Helmholtz or wave equation. [The EWM modeling applies even to non-NAH methods. For example, delay-and-sum beamforming (Van Veen and Buckley, 1988) models a field as a superposition of incoming plane waves from various directions.] In NAH, a weighted set of wave functions whose superposition accurately represents a field generated by a vibrating source or sources is sought. The coefficients of these functions are calculated to best match the acoustic quantities at the hologram array in some optimal sense. For instance, in the traditional NAH method, which relies on a discrete spatial Fourier transform of hologram pressures (DFT-based NAH; see Maynard *et al*., 1985; Williams, 1999) each element in the transformed space can be considered a complex coefficient (complex strength) of a respective (normalized) wave function, either planar, cylindrical, or spherical. In the DFT process, experimental and computational noise tends to be relegated to higher-order wave functions that can be filtered, allowing for accurate reconstruction of lower-order modes.

The speed and accuracy of this approach make DFT-based NAH highly desirable, but the hologram requirements of this method can become restrictive when a field is generated by sources of complex shape, or by multiple spatially separated sources. For example, in DFT-based NAH, the hologram must be measured with regular grid spacing. The vibrating source and the hologram surface must conform to the level surface of a separable coordinate system, or, in other words, measurements must be taken over a two-dimensional surface containing a level of constant coordinates, such as a plane, cylinder, or a sphere. The hologram must also cover the source region sufficiently to measure beyond the source edges, so that the radiation features

---

[a] Author to whom correspondence should be addressed. Current address: Air Force Research Laboratory, Battlespace Acoustics Branch, Wright-Patterson AFB, Dayton, OH 45433. Electronic mail: alantwall@gmail.com

caused by discontinuities at the edges are captured and that levels drop significantly toward the boundaries of the hologram aperture. Advancements in NAH include the development of methods for sources with no level surface in a separable coordinate system (irregular sources), methods for holograms that do not conform to source surfaces (non-conformal measurements), and methods for holograms that do not fully cover the source (patch methods; see Veronesi and Maynard, 1989; Koopmann *et al.*, 1989; Huang, 1990; Bai, 1992; Wang and Wu, 1997; Steiner and Hald, 2001). Some of these methods are discussed here with emphasis on the principles that support the current application to multi-source configurations.

Veronesi and Maynard (1989) developed a finite-element approach to NAH [based on the work of Koopmann and Benner (1982)] in which the surface of a source of irregular geometry is represented by relatively small flat plates over which the acoustic pressure and normal component of the particle velocity is assumed constant. Veronesi and Maynard introduced the concept of singular value decomposition (SVD) to the field of sound field reconstructions in order to filter out numerical noise in the reconstruction, which acts in a similar manner to the removal of noise in the high-order wave functions of DFT-based NAH. Their methods were tested on a numerical simulation of a vibrating piston set into a rigid sphere. Two holograms were simulated, one using a conformal measurement geometry and a second using a planar measurement geometry. In general, they demonstrated that source models (i.e., the spatial distribution of surface patches in relation to the piston) affect reconstruction accuracy. They also showed how a conformal simulated measurement required fewer measurement points than the planar measurement to obtain reasonable results.

In another approach for irregularly shaped sources, the boundary element method (BEM) discretizes the Kirchhoff-Helmholtz integral equation into matrices representing hologram points, source nodes, and the integrals over the source surface (Huang, 1990; Bai, 1992; Fahy and Gardonio, 2007a). The BEM method either models the distribution of surface motion of a vibrating source as an array of elementary sources operating in the presence of the vibrating body itself (surface nodes, see Fahy and Gardonio, 2007b), or as a distribution of nodes on an arbitrary surface interior to the actual vibrator. Like finite-element NAH, BEM-based NAH does not require a regular grid or conformal surface in the hologram measurement. It can also incorporate an SVD to filter the noise relegated to high-order components. In a series of reconstructions of simulated sources (including that of a piston set into a sphere), it was found that finer hologram meshes (or more measurement points) in relation to the spatial wavelengths (or characteristic sizes of the field features) also resulted in more accurate reconstructions. In fact, favorable mesh densities sometimes resulted in acceptable accurate reconstructions without the use of the SVD (i.e., regularization).

The method of superposition (Koopmann *et al.*, 1989), wherein a distribution of simple sources placed inside a vibrating structure generates the equivalent pressure and velocity on source surface, provides more accurate results when the equivalent source distribution is compacted toward the center of the vibrator. This is partially because the source compaction effectively increases the sizes of spatial features on the vibrator surface in relation to the mesh of elements used to represent it.

The statistically optimized near-field acoustical holography (SONAH) algorithm uses matrices of elementary wave functions, which are evaluated at both hologram and reconstruction points, to calculate a transfer function matrix between all hologram locations and reconstruction locations (Steiner and Hald, 2001). It calculates an SVD on the hologram cross-spectral matrix to facilitate regularization, then applies the regularized transfer functions to the measured hologram pressures to obtain the reconstructed field. The elementary functions can be planar (Steiner and Hald, 2001), cylindrical (Cho *et al.*, 2005), or spherical. Hald (2005) used SONAH when he created a randomly spaced array that could perform both beamforming and NAH to obtain low and high frequency reconstructions. In a similar approach to SONAH, the Helmholtz equation least squares (HELS) algorithm utilizes a least-squares fitting of a linear combination of (typically) single-origin multipole functions (spherical wave functions) to data measured by the hologram array (Wang and Wu, 1997). The HELS method has been expanded to incorporate spatial distributions of multipoles for source configurations that are not easily approximated by wave functions of a single origin (Semenova and Wu, 2005; Shah *et al.*, 2011). In various studies using SONAH, HELS, and other methods, it has been found that reconstruction accuracy is improved, the need for regularization is eliminated or mitigated, and the number of necessary measurements is reduced when the source and/or field are represented by lower-order wave functions that reflect the geometry of the problem (e.g., see Veronesi and Maynard, 1989; Cho *et al.*, 2005; Semenova and Wu, 2005; Gomes *et al.*, 2007; Hald, 2014). This is in part because the elimination of higher-order terms has a regularizing effect.

Of course, wave functions from any complete basis can theoretically represent any sound field obeying the Helmholtz equation in a source-free region if enough terms are used in the expansion. Many sources have successfully been reconstructed using NAH with non-conformal wave functions (e.g., see Semenova and Wu, 2005; Gomes *et al.*, 2007; Wall *et al.*, 2012). Guidelines are sometimes provided for optimal selection and scaling of wave functions (Semenova and Wu, 2005; Hald, 2009, 2014). In addition, much work has been done to improve regularization methods to eliminate noise from ill-posed problems without compromising the evanescent wave information contained in higher-order terms [e.g., see Williams (2001) and additional references found therein] and even to simulate improved measurement arrays by the extrapolation of data in the spatial domain (Williams, 2003). When a lack of knowledge about a source *a priori* makes it difficult to infer an efficient EWM, optimization algorithms might be used to narrow down a large basis-function design space (Antoni, 2012; Hart *et al.*, 2013). However, in many cases accuracy and efficiency are improved by the incorporation of known source information into the EWM.

The principles described above can be summarized as follows. The accuracy of a sound field reconstruction from an inverse method relies heavily on (1) the ability of the wave functions to represent the field and (2) the ability of the hologram measurement to capture the spatial variation in the acoustic field to represent each expansion function. Thus, information about a source of interest, such as its location, geometry, or distribution, can be leveraged to generate an accurate source and field model. The selection of an inverse method dictates the extent of source information that can be incorporated into the model.

The application of these principles to reconstruct the sound fields of multiple sources of various shapes and separated in space is the objective of this paper. It utilizes the SONAH algorithm in a way similar to that of Hald (2006), who used a measurement of two parallel planar arrays to separate incoming and outgoing waves. The idea of wave separation using parallel arrays was not new [see Weinreich and Arnold (1980) and Tamura (1990)], but Hald introduced its implementation into the SONAH algorithm by representing the incoming and outgoing waves with two distinct wave function matrices, which were concatenated prior to field reconstruction. This method was further investigated for accuracy in the reconstruction of both pressure and particle velocity by Jacobsen *et al.* (2008). The current paper builds upon Hald's approach to utilize the flexibility of the SONAH algorithm for an EWM that incorporates multiple types of sources of arbitrary shape. The method presented here employs an EWM where a sound field is represented as a combination of multiple sets of elementary wave functions, each set for a single source shape and location. Insomuch as each set of wave functions accurately represents its respective source, the total EWM is an efficient reduced-order model for the total field. Similarly, insomuch as the aperture of the hologram array sufficiently covers the spatial region of each wave function, the hologram is sufficient to measure all components of the total sound field. A matrix concatenation scheme is used to include all wave functions in the calculation of the transfer function matrix. Thus, the EWM is generalized to represent sound fields generated by arbitrary configurations of multiple sound sources or scattering bodies with various shapes and/or locations within the field. The concatenated matrix is formatted for use in the SONAH algorithm, which provides a unique reconstruction that is optimal in a least-norm or least-squares sense. This is called multisource statistically optimized near-field acoustical holography (M-SONAH). Note that it is not within the scope of this paper to determine an optimal EWM for an arbitrary source configuration. Rather, this paper presents a method to facilitate a user-defined reduced-order approach to complicated sound fields.

Before the discussion of M-SONAH, it is important to distinguish between the multisource approach taken here and partial field decomposition (PFD). In the case of multiple incoherent sources, regardless of their relative locations, a PFD must be performed to separate the partially coherent field into mutually incoherent partial fields prior to NAH projection (Hald, 1989; Lee and Bolton, 2006). The current method is not intended to replace PFD, since it still requires a self-coherent hologram. If the multiple sources of interest are independent radiators, then M-SONAH will need to be used in conjunction with PFD.

In Sec. II, the underlying theory of M-SONAH is presented in detail, specifying the modification to the SONAH algorithm that incorporates a flexible EWM. In Sec. III, two numerical experiments are performed with configurations of multiple sources, which experiments demonstrate the implementation of M-SONAH. For comparison, the same fields are reconstructed using SONAH based on an EWM including only plane wave functions (Hald, 2009) and SONAH based on a strictly cylindrical EWM (Cho *et al.*, 2005). Reconstruction results for the various experiments are given in Sec. IV, which show the advantages of M-SONAH, including its accuracy and convenience, for multisource applications. Section V contains a discussion of considerations for the implementation of M-SONAH, a summary of its advantages, and its potential for further use.

II. THEORY

The M-SONAH method is an extension of SONAH. Thus, only a basic outline for its algorithm is given here, including the multisource EWM approach and concatenation scheme. For additional details on the SONAH processing, the reader is referred to Hald (2009) and Hald (2014), who specifies recommended EWM parameters, a description of spatial aliasing, wave-number domain leakage, regularization, and the extension of the algorithm to calculate particle velocity.

It is assumed that the complex, time-harmonic sound field has been measured at a set of locations $\mathbf{r}_h, h = 1, 2, \ldots, I$, on the hologram, Ω (not necessarily a two-dimensional surface), in a source-free region that obeys the Helmholtz equation. A technique of reconstructing sound pressures at locations $\mathbf{r}_q, q = 1, 2, \ldots, Q$ on surface Γ, from hologram pressures, is explained. A set of wave functions, $\Psi_n, n = 1, 2, \ldots, N$ are chosen that are solutions to the Helmholtz equation in the source-free field. The wave functions can be elementary functions associated with planar, cylindrical, or spherical geometries, or they can be derived from knowledge of the source properties (outside the source-free region). The complex pressures at both Ω and Γ are expressed in terms of the same linear combinations of basis functions, Ψ_n.

First, the hologram pressures on Ω may be expanded as

$$p(\mathbf{r}_h) = \sum_{n=1}^{N} g_n \Psi_n(\mathbf{r}_h)\,, \quad h = 1, \ldots, I, \tag{1}$$

where g_n are the complex expansion coefficients for the wave functions. In any NAH process, the goal is to determine the complex coefficients that most accurately represent the measured pressures at the measurement array. For SONAH, Eq. (1) is represented in matrix form,

$$\mathbf{D}\mathbf{g} = \mathbf{p}(\mathbf{r}_h), \tag{2}$$

where

$$\mathbf{p}(\mathbf{r}_h) \equiv [p(\mathbf{r}_h)] \equiv \begin{bmatrix} p(\mathbf{r}_1) \\ p(\mathbf{r}_2) \\ \vdots \\ p(\mathbf{r}_I) \end{bmatrix}, \quad \text{and} \quad \mathbf{g} \equiv [g_n] \equiv \begin{bmatrix} g_1 \\ g_2 \\ \vdots \\ g_N \end{bmatrix}. \tag{3}$$

The matrix of wave functions evaluated at the measurement positions is $\mathbf{D}$, and its transpose ($\mathbf{A}' = \mathbf{D}^{\mathrm{T}}$) is defined as

$$\mathbf{A}' \equiv [\Psi_n(\mathbf{r}_h)] \equiv \begin{bmatrix} \Psi_1(\mathbf{r}_1) & \Psi_1(\mathbf{r}_2) & \cdots & \Psi_1(\mathbf{r}_I) \\ \Psi_2(\mathbf{r}_1) & \Psi_2(\mathbf{r}_2) & & \Psi_2(\mathbf{r}_I) \\ \vdots & & \ddots & \vdots \\ \Psi_N(\mathbf{r}_1) & \Psi_N(\mathbf{r}_2) & \cdots & \Psi_N(\mathbf{r}_I) \end{bmatrix}. \tag{4}$$

It is helpful to note that, although DFT-based NAH does not include the manual formulation of a wave function matrix, the same information is represented by complex wave function coefficients in the wave number domain that result from the DFT processing. In SONAH, the wave function set, $\mathbf{A}'$, must be defined by the user.

It is valuable to discuss the wave function matrix in terms of completeness. Usually, the set of wave functions is chosen from a complete basis—an infinite set of functions whose superposition could represent any sound field that obeys the Helmholtz equation. It is theoretically possible to use any complete set of functions to represent a non-conformal source (e.g., plane waves to represent a compact spherical source), but the hologram array and processing requirements (e.g., the number of terms required) would be prohibitive in many circumstances. In practice, a finite subset of functions is used to provide an approximation of the sound field. It is more efficient and practical to choose a conformal set. The desire to limit the number of wave functions is one reason why plane waves are used to represent extended, flat sources, spherical waves are used for compact sources, etc. Hald (2009) provides guidelines for the selection of a sufficient set for a given hologram grid.

The basis functions, Ψ_n, that are typically employed in the EWM used in SONAH are elementary wave functions limited to a single separable coordinate system, such as plane waves (Hald, 2009), cylindrical waves (Cho *et al.*, 2005), or spherical waves, chosen to conform to the surface shape of the vibrator. When a distribution of sources, or a multicomponent source, is under investigation they may not lend themselves to such a convenient representation. In many instances, the array aperture and density requirements, and the necessary number of terms in the EWM from a single, orthogonal, complete basis set would be stringent enough to prohibit successful sound field reconstruction. Hence, it is desirable to find a reduced-order representation of a sound field for complicated source configurations. This motivates the incorporation of the multisource type EWM into the SONAH algorithm that is presented here.

The transfer function formulation of SONAH allows for a reduced-order approach for multiple sources. If multiple components of a source, or multiple sources of various shapes exist then multiple sets of wave functions conformal to each individual source can be included in the EWM formulation of Eq. (4). These might include combinations of planar, cylindrical, and spherical functions.

In the M-SONAH formulation, the wave function matrix of Eq. (4) is extended to include multiple sets of wave functions. A set of wave function values at the I positions on Ω can be defined for each source type, s, and written as the matrix

$$\mathbf{B}_s \equiv [\Psi_n^s(\mathbf{r}_h)] \equiv \begin{bmatrix} \Psi_1^s(\mathbf{r}_1) & \Psi_1^s(\mathbf{r}_2) & \cdots & \Psi_1^s(\mathbf{r}_I) \\ \Psi_2^s(\mathbf{r}_1) & \Psi_2^s(\mathbf{r}_2) & & \Psi_2^s(\mathbf{r}_I) \\ \vdots & & \ddots & \vdots \\ \Psi_N^s(\mathbf{r}_1) & \Psi_N^s(\mathbf{r}_2) & \cdots & \Psi_N^s(\mathbf{r}_I) \end{bmatrix}. \tag{5}$$

The wave functions need not be of the same type nor of the same number, N, for each source. The wave function matrices for all S sources are then concatenated vertically to obtain the composite matrix

$$\mathbf{A} = \begin{bmatrix} \mathbf{B}_1 \\ \mathbf{B}_2 \\ \vdots \\ \mathbf{B}_S \end{bmatrix}. \tag{6}$$

The total number of wave functions across all S sets is called M. The problem of solving Eq. (2) is now akin to solving I equations with M unknowns. If $I > M$, the problem is over-determined, and generally no exact solution can be found. In such a case, the solution that approximates the exact solution with the least error is called the least-squares solution (Moon and Stirling, 2000), the coefficients for which are

$$\mathbf{g} = (\mathbf{D}^{\mathrm{H}}\mathbf{D})^{-1}\mathbf{D}^{\mathrm{H}}\mathbf{p}(\mathbf{r}_h), \tag{7}$$

where H represents the Hermitian transpose. If $I < M$, the problem is under-determined, and there are an infinite number of solutions. In order to solve the problem uniquely, a reasonable criterion is to find the solution of smallest norm, called the least-norm solution (Moon and Stirling, 2000), for which the coefficients are

$$\mathbf{g} = \mathbf{D}^{\mathrm{H}}(\mathbf{D}\mathbf{D}^{\mathrm{H}})^{-1}\mathbf{p}(\mathbf{r}_h). \tag{8}$$

In NAH applications, the selection of a sufficient set of wave functions almost inevitably leads to a number of wave functions, M, greater than the number of measurement positions, I. Hence, we will proceed with the least-norm solution, which is computationally more efficient to calculate. Proceeding with the least-norm solution, Eq. (8) may be written equivalently as

$$\mathbf{g} = \mathbf{A}^*(\mathbf{A}^{\mathrm{T}}\mathbf{A}^*)^{-1}\mathbf{p}(\mathbf{r}_h), \tag{9}$$

where * signifies the complex conjugate, or

$$\mathbf{g}^{\mathrm{T}} = \mathbf{p}^{\mathrm{T}}(\mathbf{r}_h)(\mathbf{A}^{\mathrm{H}}\mathbf{A})^{-1}\mathbf{A}^{\mathrm{H}}. \tag{10}$$

Solving Eq. (8) is complicated by spatial noise in $\mathbf{p}(\mathbf{r}_h)$, for example, from slight mispositioning of field microphones during a measurement. This produces a "noise floor" in the matrix inversion of $\mathbf{A}^{\mathrm{H}}\mathbf{A}$, which causes the coefficients calculated in Eq. (10) to diverge, introducing large errors into the field reconstruction. Hence, regularization is necessary prior to calculation of the inverse in Eq. (10). There is no all-encompassing regularization technique that is optimal for every inverse problem. However, Williams (2001) investigated several methods and showed that the combination of modified Tikhonov regularization, in conjunction with the generalized cross-validation (GCV) procedure for the selection of the regularization parameter, had the best performance for many realizations of his NAH problem. Thus, it is commonly employed in NAH applications, including the SONAH formulation by Cho *et al.* (2005). Modified Tikhonov is the regularization method used in this work, and it is summarized here.

We seek a regularized inverse of $\mathbf{A}^{\mathrm{H}}\mathbf{A}$ in order to calculate $\mathbf{g}^{\mathrm{T}}$ in Eq. (10). The matrix $\mathbf{A}^{\mathrm{H}}\mathbf{A}$ is positive semi-definite Hermitian, so it may be represented by the symmetric SVD

$$\mathbf{A}^{\mathrm{H}}\mathbf{A} = \mathbf{V}\mathbf{G}\mathbf{V}^{\mathrm{H}}, \tag{11}$$

where $\mathbf{V}$ is a matrix of singular vectors and the diagonal elements of $\mathbf{G}$ are the singular values. Then, the regularized inverse of $\mathbf{A}^{\mathrm{H}}\mathbf{A}$ is

$$\mathbf{R}_{\mathbf{A}^{\mathrm{H}}\mathbf{A}} = \mathbf{V}[\alpha(\mathbf{F}_1^{\alpha})^2 + \mathbf{G}^{\mathrm{H}}\mathbf{G}]^{-1}\mathbf{G}^{\mathrm{H}}\mathbf{V}^{\mathrm{H}}. \tag{12}$$

Here, the singular values are high-pass filtered by the modified Tikhonov filter,

$$\mathbf{F}_1^{\alpha} = \mathrm{diag}\left[\ldots, \alpha \Big/ \left[\alpha + |\lambda_j|^2\left(\frac{\alpha + |\lambda_j|^2}{\alpha}\right)^2\right], \ldots\right], \tag{13}$$

and where the terms λ_j are the singular values (diagonal elements of $\mathbf{G}$). The GCV method can be used to find the regularization parameter, α, by minimizing the cost function

$$J(\alpha) \equiv \frac{\|\mathbf{F}_1^{\alpha}\mathbf{V}^{\mathrm{H}}\mathbf{p}(\mathbf{r}_h)\|^2}{[\mathrm{trace}\,(\mathbf{F}_1^{\alpha})]^2}. \tag{14}$$

With the regularization complete, the inverse term, $(\mathbf{A}^{\mathrm{H}}\mathbf{A})^{-1}$, of Eq. (10) may be replaced with the regularized inverse, $\mathbf{R}_{\mathbf{A}^{\mathrm{H}}\mathbf{A}}$, and the expansion coefficients are now given by

$$\tilde{\mathbf{g}}^{\mathrm{T}} = \mathbf{p}^{\mathrm{T}}(\mathbf{r}_h)\mathbf{R}_{\mathbf{A}^{\mathrm{H}}\mathbf{A}}\mathbf{A}^{\mathrm{H}}. \tag{15}$$

These regularized coefficients can now be used to represent field pressures in terms of the wave functions. Hence, the reconstructed pressure at a desired location $\mathbf{r}_q$ on Γ can be written as the linear combination of wave functions,

$$p(\mathbf{r}_q) = \sum_{n=1}^{N} \tilde{g}_n \Psi_n(\mathbf{r}_q)\,,\ q = 1, 2, \ldots, Q, \tag{16}$$

where $\tilde{g}_n$ are the elements of $\tilde{\mathbf{g}}$. Since all the terms of Eq. (16) fulfill the Helmholtz equation, the reconstructed field does as well. Equation (16) can be recast in matrix form as

$$\mathbf{p}(\mathbf{r}_q) = \tilde{\mathbf{g}}^{\mathrm{T}}\boldsymbol{\alpha}\,, \tag{17}$$

where $\boldsymbol{\alpha}$ is the matrix of wave function values at all reconstruction locations and is defined as

$$\boldsymbol{\alpha} \equiv \begin{bmatrix} \boldsymbol{\beta}_1 \\ \boldsymbol{\beta}_2 \\ \vdots \\ \boldsymbol{\beta}_S \end{bmatrix}. \tag{18}$$

The elements of $\boldsymbol{\alpha}$ are the same wave functions found in $\mathbf{A}$, now evaluated at the Q reconstruction points on Γ,

$$\boldsymbol{\beta}_s \equiv [\Psi_n^s(\mathbf{r}_q)] \equiv \begin{bmatrix} \Psi_1^s(\mathbf{r}_1) & \Psi_1^s(\mathbf{r}_2) & \cdots & \Psi_1^s(\mathbf{r}_Q) \\ \Psi_2^s(\mathbf{r}_1) & \Psi_2^s(\mathbf{r}_2) & & \Psi_2^s(\mathbf{r}_Q) \\ \vdots & & \ddots & \vdots \\ \Psi_N^s(\mathbf{r}_1) & \Psi_N^s(\mathbf{r}_2) & \cdots & \Psi_N^s(\mathbf{r}_Q) \end{bmatrix}. \tag{19}$$

Finally, the SONAH formulation for the reconstructed pressures is found by combining Eq. (15) with Eq. (17) to obtain

$$\mathbf{p}(\mathbf{r}_q) = \mathbf{p}^{\mathrm{T}}(\mathbf{r}_h)\,\mathbf{R}_{\mathbf{A}^{\mathrm{H}}\mathbf{A}}\mathbf{A}^{\mathrm{H}}\boldsymbol{\alpha}, \tag{20}$$

where $\mathbf{p}^{\mathrm{T}}(\mathbf{r}_h)$ is a vector of dimensions $1 \times I$, $\mathbf{R}_{\mathbf{A}^{\mathrm{H}}\mathbf{A}}$ is $I \times I$, $\mathbf{A}^{\mathrm{H}}$ is $I \times M$, and $\boldsymbol{\alpha}$ is $M \times Q$, resulting in a reconstruction matrix $\mathbf{p}(\mathbf{r}_q)$ of size $1 \times Q$.

It is beneficial to discuss some of the advantages of the M-SONAH method, as well as some considerations that can guide the reader in its appropriate use. The first advantage is that this method provides for a convenient, reduced-order representation of sound fields generated by multiple sources of various shapes and locations for which other NAH methods could fail. In the event that a low-order EWM is not feasible, myriad NAH methods have been developed to measure complicated sources with high accuracy in limited regions, or with greater computational costs (Huang, 1990; Bai, 1992; Rayess and Wu, 2000; Semenova and Wu, 2005; Sarkissian, 2005; Shah *et al.*, 2011). When it is difficult to infer information about a source, optimization schemes might be used to narrow down an acceptably accurate EWM within a broader design space (Antoni, 2012). However, to paraphrase Mollo-Christensen (1967), "If you think you know some of the features of a [source], for goodness sake put it in [the model]." Knowledge of the approximate locations and shapes of vibrators can allow the user to reduce the number of wave functions required to describe them by orders of magnitude, can increase reconstruction accuracy, and can reduce the number of measurement points.

It is also important to understand that while a field can be represented using a non-conformal basis set if the near-field evanescent wave information is captured, a more accurate result can be obtained if the wave functions match the source geometry. For example, ESM approaches to sound field visualization based on estimations of source distributions have made the measurement of very large, complicated, even incoherent sources much more feasible (Shah *et al.*, 2011; Morgan *et al.*, 2012; Hart *et al.*, 2013). In a similar manner, M-SONAH allows a user the necessary flexibility to incorporate knowledge of the source in the model.

III. NUMERICAL EXPERIMENTS

Two numerical experiments were performed to demonstrate the use and capabilities of M-SONAH. First, the near-field of two simulated sources of different shapes—a vibrating piston set into a rigid sphere and a finite line array—were reconstructed with M-SONAH. For comparison, planar SONAH (Hald, 2009) was also implemented. This simulation demonstrates the increased accuracy that can be obtained by incorporation of knowledge about the source into the EWM. In the second experiment, a measurement was simulated far from the source plane of two parallel, finite line arrays. This simulation was motivated by past NAH investigations of a long, military jet noise source in the presence of a rigid ground reflection (Wall, 2013; Wall *et al.*, 2013a, 2013b). Here, M-SONAH, planar SONAH, and cylindrical SONAH (Cho *et al.*, 2005) are all used to reconstruct the field to demonstrate the capabilities of M-SONAH when the hologram is far from the source.

The determination of the wave function sets is a two-step process. First, the types of wave functions used in an EWM must be selected. Table I lists three types of wave functions that can be used. The planar wave function, $\Phi^{\mathrm{pl}}_{k_y,k_z}$, is given as a function of Cartesian coordinates x, y, and z, and x_0 specifies the virtual source plane. The coordinate-specific wave numbers k_x, k_y, and k_z, are constrained by

$$k_x = \begin{cases} \sqrt{k^2 - (k_y^2 + k_z^2)} & \text{for} \quad k^2 \geq (k_y^2 + k_z^2) \\ i\sqrt{(k_y^2 + k_z^2) - k^2} & \text{for} \quad k^2 < (k_y^2 + k_z^2), \end{cases} \tag{21}$$

where $k = \omega/c$ is the acoustic wave number, ω is the angular frequency, and c is the ambient sound speed, which is 343 m/s in these simulations. This formulation implies an assumed time harmonicity (excluded from all wave functions of Table I) of $e^{-i\omega t}$, where t represents time. The weighting function $F(k_x)$ enforces a constant *directional* power density (Hald, 2009), and is defined as $F(k_x) = \sqrt{k/|k_x|}$. Cylindrical wave functions for outward propagating waves can be expressed in terms of Hankel functions and complex exponentials as $\Phi^{\mathrm{cyl}}_{\ell,k_z}$ in Table I, where r, ϕ, and z are the spatial coordinates, $H^{(1)}_\ell$ is the ℓth-order Hankel function of the first kind, r_0 is some small reference radius (traditionally the assumed source radius), and the radial wavenumber is

$$k_r = \begin{cases} \sqrt{k^2 - k_z^2} & \text{for} \quad |k| \geq |k_z|, \\ i\sqrt{k_z^2 - k^2} & \text{for} \quad |k| < |k_z|. \end{cases} \tag{22}$$

Lastly, spherical wave functions for outward propagating waves are defined as $\Phi^{\mathrm{sph}}_{m,\ell}$ in Table I as a function of spherical coordinates ρ, θ, and ϕ, and $P^m_\ell(\cos\theta)$ are the associated Legendre functions of degree ℓ and order m.

TABLE I. Wave function definitions in planar, cylindrical, and spherical coordinates.

Planar	$\Phi^{\mathrm{pl}}_{k_y,k_z}(x,y,z) \equiv F(k_x)e^{i(k_y y + k_z z + k_x(x - x_0))}$
Cylindrical	$\Phi^{\mathrm{cyl}}_{\ell,k_z}(r,\phi,z) \equiv \dfrac{H^{(1)}_\ell(k_r r)}{H^{(1)}_\ell(k_r r_0)} e^{i\ell\phi} e^{ik_z z}, \quad r \geq r_0$
Spherical	$\Phi^{\mathrm{sph}}_{m,\ell}(\rho,\theta,\phi) \equiv H^{(1)}_\ell(kr)P^m_\ell(\cos\theta)e^{im\phi}$

In the second step, the wave function sets used in the EWM must be specified according to the source locations within the coordinate system. The EWMs of the current simulations are comprised of combinations of the wave functions defined in Table I. These wave function sets are outlined in Table II, including the necessary equations to transform from Cartesian coordinates to the respective coordinates used in each wave function calculation, and the degrees, orders, and coordinate-specific wave numbers included in each set. First, a set of spherical wave functions is defined for hologram points as $\mathbf{B}_1$ and for reconstruction points as $\boldsymbol{\beta}_1$ in Table II. The origin of these functions is defined to be $(x,y,z) = (-0.2,\ -0.5,\ 0.0\,\mathrm{m})$. Associated Legendre functions of degree $\ell = 0$ through 10, and associated Legendre function and Hankel function orders $m = -\ell$ through ℓ are included. Next, two sets of cylindrical wave functions are defined in Table II. The set specified by $\mathbf{B}_2$ and $\boldsymbol{\beta}_2$ is centered on the Cartesian origin $(x,y,z) = (0.0,\ 0.5,\ 0.0\,\mathrm{m})$, and the set specified by $\mathbf{B}_3$ and $\boldsymbol{\beta}_3$ is centered on $(x,y,z) = (0.0,\ -0.5,\ 0.0\,\mathrm{m})$. The sources that will be represented here by cylindrical wave functions are axisymmetric, so both sets $\mathbf{B}_2$ and $\mathbf{B}_3$ include only Hankel function orders of $\ell = 0$. The hologram grid geometries, defined later, motivate a range of z-coordinate wave numbers, k_z, from $-2\pi/0.15\,\mathrm{m}^{-1}$ to $+2\pi/0.15\,\mathrm{m}^{-1}$, with a regular spacing of $\Delta k_z = \pi/2.0\,\mathrm{m}^{-1}$. Finally, the planar wave function set is defined by $\mathbf{B}_4$ and $\boldsymbol{\beta}_4$ in Table II, with wave numbers k_y and k_z defined similarly to those of k_z in the cylindrical sets.

TABLE II. Four wave function sets designed for the specific simulated source configurations used in experiments of the current paper.

Set of spherical functions

$\mathbf{B}_1 \equiv [\Phi^{\text{sph}}_{m,\ell}(\mathbf{r}_h)]$ and $\boldsymbol{\beta}_1 \equiv [\Phi^{\text{sph}}_{m,\ell}(\mathbf{r}_q)]$, where

$\Phi^{\text{sph}}_{m,\ell}(\mathbf{r}) = \Phi^{\text{sph}}_{m,\ell}(\rho, \theta, \phi)$

$\rho = \sqrt{(x + 0.2\,\text{m})^2 + (y + 0.5\,\text{m})^2 + z^2}$

$\theta \equiv \cos^{-1}\left(\frac{x + 0.2\,\text{m}}{\rho}\right)$

$\phi \equiv \tan^{-1}\left(\frac{z}{y + 0.5\,\text{m}}\right)$, four-quadrant arctangent with range $(-\pi, \pi]$

$\ell = 0, 1, \ldots, 10$

$m = -\ell, -(\ell - 1), \ldots, \ell - 1, \ell$

First set of cylindrical functions

$\mathbf{B}_2 \equiv [\Phi^{\text{cyl}}_{\ell,k_z}(\mathbf{r}_h)]$ and $\boldsymbol{\beta}_2 = [\Phi^{\text{cyl}}_{\ell,k_z}(\mathbf{r}_q)]$, where

$\Phi^{\text{cyl}}_{\ell,k_z}(\mathbf{r}) = \Phi^{\text{cyl}}_{\ell,k_z}(r, \phi, z)$

$r \equiv \sqrt{x^2 + (y - 0.5\,\text{m})^2}$

$\phi \equiv \tan^{-1}\left(\frac{y - 0.5\,\text{m}}{x}\right)$, four-quadrant arctangent with range $(-\pi, \pi]$

$z \equiv z$

$\ell = 0$

$\Delta k_z = \pi/2.0\,\text{m}^{-1}$, $|k_z|_{\max} = 2\pi/0.15\,\text{m}^{-1}$

Second set of cylindrical functions

$\mathbf{B}_3 \equiv [\Phi^{\text{cyl}}_{\ell,k_z}(\mathbf{r}_h)]$ and $\boldsymbol{\beta}_3 = [\Phi^{\text{cyl}}_{\ell,k_z}(\mathbf{r}_q)]$, where

$\Phi^{\text{cyl}}_{\ell,k_z}(\mathbf{r}) = \Phi^{\text{cyl}}_{\ell,k_z}(r, \phi, z)$

$r \equiv \sqrt{x^2 + (y + 0.5\,\text{m})^2}$

$\phi \equiv \tan^{-1}\left(\frac{y + 0.5\,\text{m}}{x}\right)$, four-quadrant arctangent with range $(-\pi, \pi]$

$z \equiv z$

$\ell = 0$

$\Delta k_z = \pi/2.0\,\text{m}^{-1}$, $|k_z|_{\max} = 2\pi/0.15\,\text{m}^{-1}$

Set of planar functions

$\mathbf{B}_4 \equiv [\Phi^{\text{pl}}_{k_y,k_z}(\mathbf{r}_h)]$ and $\boldsymbol{\beta}_4 = [\Phi^{\text{pl}}_{k_y,k_z}(\mathbf{r}_q)]$, where

$\Phi^{\text{pl}}_{k_y,k_z}(\mathbf{r}) = \Phi^{\text{pl}}_{k_y,k_z}(x, y, z)$

$\Delta k_y \equiv \pi/2.0\ \text{m}^{-1}$, $|k_y|_{\max} = 2\pi/0.15\,\text{m}^{-1}$

$\Delta k_z \equiv \pi/2.0\ \text{m}^{-1}$, $|k_z|_{\max} = 2\pi/0.15\,\text{m}^{-1}$

A. Piston in a sphere and line array

Figure 1 illustrates the source configuration of the first simulation. First, a vibrating piston set into a rigid sphere (approximated as a small, spherical cap) was simulated. The analytical formula for radiation from a piston in a sphere is provided by Morse and Ingard (1968). The sphere radius was chosen to be $a = 0.2\,\text{m}$, the sphere was centered at $(x, y, z) = (-0.2,\ -0.5,\ 0.0\,\text{m})$, the piston was on top of the sphere (near $x = 0\,\text{m}$), and the effective radius of the piston was $d = 0.05\,\text{m}$. For the second source, a line array of 51 monopoles was simulated along $(x, y) = (0.0, 0.5\,\text{m})$, spanning from $z = -0.5$ to $0.5\,\text{m}$. A Gaussian weighting was applied to the amplitudes of the monopoles along each array, with (non-dimensional) source strengths as a function of z defined as

$$W(z) = e^{-(z^2/2\sigma^2)}, \tag{23}$$

where $\sigma = 0.25\,\text{m}$. Field pressures from the line array were simulated with the free-space Green's function. Both the piston-in-sphere and line-array sources radiated at 1 kHz ($ka = 3.7$ for the piston), and the field pressures from the two sources were summed coherently to obtain the total field.

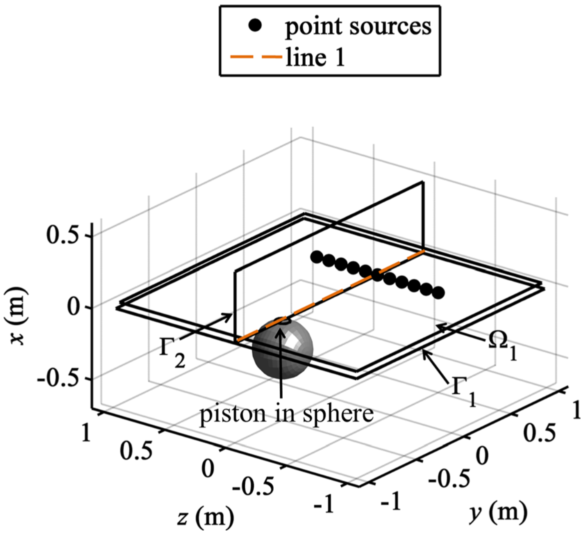

FIG. 1. (Color online) Diagram of the vibrating piston-in-sphere plus line-array simulation. Line array includes 51 monopole sources, and is not to scale. Hologram surface Ω_1 is at $x = 0.05\,\text{m}$, reconstruction surface Γ_1 is at $x = -0.001\,\text{m}$, and reconstruction surface Γ_2 is placed vertically, running directly above the centers of each source.

The simulated hologram and reconstruction surfaces are shown relative to the sources in Fig. 1. The hologram surface, Ω_1, was located at $x = 0.05\,\text{m}$. Measurements were simulated with a regular 0.15 m grid spacing over Ω_1. The surface spanned a $2\,\text{m} \times 2\,\text{m}$ area, and was centered on the $y - z$ origin. In addition, benchmark measurements were simulated at reconstruction surface Γ_1, which was located at $x = -0.001\,\text{m}$ (just below the source plane to avoid singularities at the monopoles) and spanned the same $y - z$ area as Ω_1, and at Γ_2, which was placed vertically (in the $x - y$ plane) and ran directly above the centers of the piston-in-sphere and line-array sources.

The field was reconstructed using the data from hologram Ω_1 and the M-SONAH method. The EWM used included the spherical wave function set to represent radiation from the piston in the sphere, and the first cylindrical set to represent the line array. Thus, the EWM matrices were expressed as

$$\mathbf{A}_{1,\text{M-SONAH}} = \begin{bmatrix} \mathbf{B}_1 \\ \mathbf{B}_2 \end{bmatrix} \text{ and } \boldsymbol{\alpha}_{1,\text{M-SONAH}} = \begin{bmatrix} \boldsymbol{\beta}_1 \\ \boldsymbol{\beta}_2 \end{bmatrix}. \tag{24}$$

Concurrently, a reconstruction was made using the same data from Ω_1, but with a strictly planar SONAH approach, whose EWM was formulated as

$$\mathbf{A}_{1,\text{pl}} = \mathbf{B}_4, \text{ and } \boldsymbol{\alpha}_{1,\text{pl}} = \boldsymbol{\beta}_4. \tag{25}$$

Reconstructions from the two methods are shown in Sec. IV A.

B. Two line arrays

The second simulation setup is illustrated in Fig. 2. Here, the source configuration includes two parallel, coherent, linear

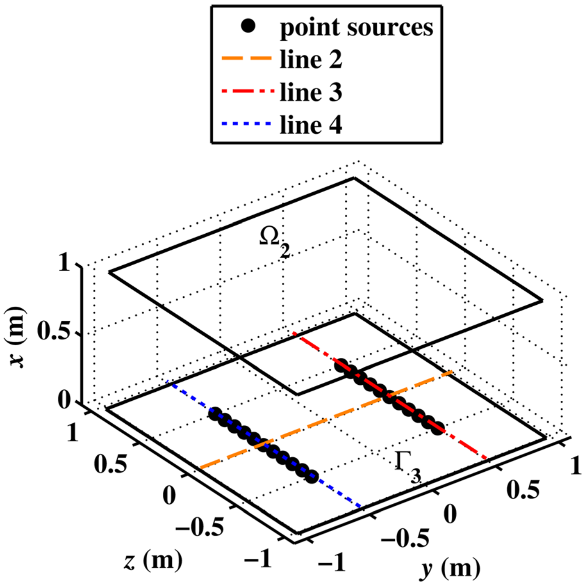

FIG. 2. (Color online) Diagram of the two-line-array simulation. Each line array includes 51 monopole sources, and is not to scale. Hologram surface Ω_2 is at $x = 1.0$ m, and reconstruction surface Γ_3 is at $x = -0.01$ m.

arrays a distance of 1.0 m apart in the $y - z$ plane. One line array was identical to that of the previous simulation, and the second line array was identical to the first, but was placed along $(x, y) = (0.0, -0.5\,\text{m})$, spanning from $z = -0.5$ to 0.5 m.

Again, field pressures were calculated with the free-space Green's function, sources radiated at 1 kHz, and the pressures from the two sources were summed coherently.

In this simulation, the hologram, Ω_2, was not measured in the acoustic near field. Rather, it was located at $x = 1.0$ m, about 2.9 acoustic wavelengths away from the source plane (see Fig. 2). Similar to Ω_1 in the previous example, Ω_2 contained a regular grid of measurements with equal 0.15 m spacing, spanned a 2 m × 2 m area, and was centered on the $y - z$ origin. For comparison, benchmark measurements were simulated at $\Gamma_3 = -0.01$ m.

The field was reconstructed using the M-SONAH method and data from Ω_2. The M-SONAH EWM included both sets of cylindrical functions to represent radiation from each line array, giving EWM matrices

$$\mathbf{A}_{2,\text{M–SONAH}} = \begin{bmatrix} \mathbf{B}_2 \\ \mathbf{B}_3 \end{bmatrix} \quad \text{and} \quad \boldsymbol{\alpha}_{2,\text{M–SONAH}} = \begin{bmatrix} \boldsymbol{\beta}_2 \\ \boldsymbol{\beta}_3 \end{bmatrix}. \tag{26}$$

Planar SONAH was also implemented, with EWM matrices

$$\mathbf{A}_{2,\text{pl}} = \mathbf{B}_4 \quad \text{and} \quad \boldsymbol{\alpha}_{2,\text{pl}} = \boldsymbol{\beta}_4. \tag{27}$$

For this simulation, a third approach was taken, using a strictly cylindrical SONAH approach. The EWM used in cylindrical SONAH was formulated as

$$\mathbf{A}_{2,\text{cyl}} = \mathbf{B}_2 \quad \text{and} \quad \boldsymbol{\alpha}_{2,\text{cyl}} = \boldsymbol{\beta}_2. \tag{28}$$

Thus, only the radiation from one of the two source locations was represented in the EWM. Reconstructions from the three methods are shown in Sec. IV B.

IV. RESULTS

A. Piston in a sphere and line array

All level results shown are calculated relative to the maximum pressure on the hologram, p_{max}. In the case of the piston-in-sphere plus line-array, sound pressure levels (SPLs) simulated at the hologram, Ω_1, are shown in Fig. 3(a). To simulate measurement noise, random variations in the complex pressures (real and imaginary parts) were introduced into the hologram data, such that the signal-to-noise ratio (SNR) between the maximum level and the mean noise-floor level was approximately 30 dB. Note the presence of the interference pattern due to the coherence of the two sources. Although a dense sampling is represented in Fig. 3(a), actual simulated hologram data used in the NAH projections were limited to those marked by dots. The benchmarks at Γ_1 and Γ_2 are provided in Fig. 3(b), which exhibit a similar interference pattern.

The reconstruction of the field that was calculated with M-SONAH is shown in Fig. 4. Figure 4(a) shows reconstructed SPLs at Γ_1 and Γ_2. In a comparison of Fig. 4(a) with Fig. 3(b), M-SONAH reconstructed levels are visually similar to those of the benchmarks. For a more detailed inspection, benchmark and reconstruction SPLs from a line that runs through the center of Γ_1 (along $z = 0.0$ m and $x = -0.001$ m), marked by line 1 in Fig. 1, are shown in Fig. 4(b). Circles denote the benchmark levels, and reconstruction levels are shown by the solid line. The dashed line

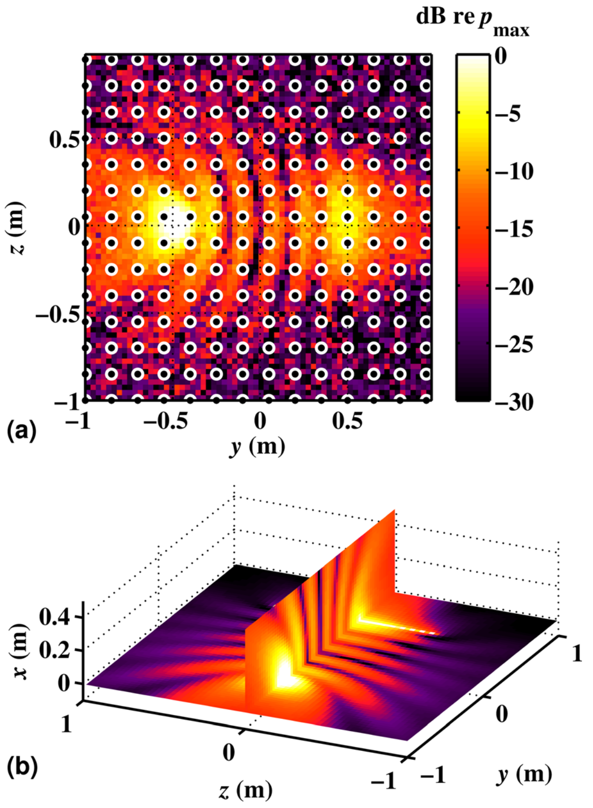

FIG. 3. (Color online) (a) Simulated SPLs at hologram Ω_1 for the piston-in-sphere plus line-array experiment. The dots show the locations of the hologram data used in reconstructions. (b) Simulated SPLs at Γ_1 and Γ_2 (benchmarks). The color bar applies to both (a) and (b).

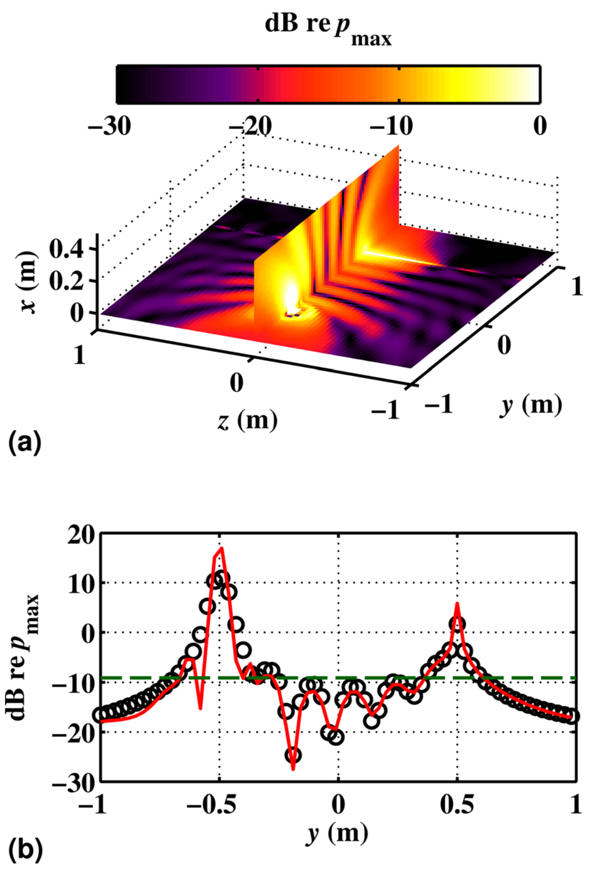

FIG. 4. (Color online) (a) Reconstructed SPLs at Γ_1 and Γ_2 after implementation of M-SONAH. (b) A comparison of select M-SONAH reconstructed SPLs (solid line) and benchmark SPLs (circles) within Γ_1, over reconstruction line 1 (at $z = 0$ m, $x = -0.001$ m). The dashed line marks the level that is 20 dB below the maximum benchmark level along line 1.

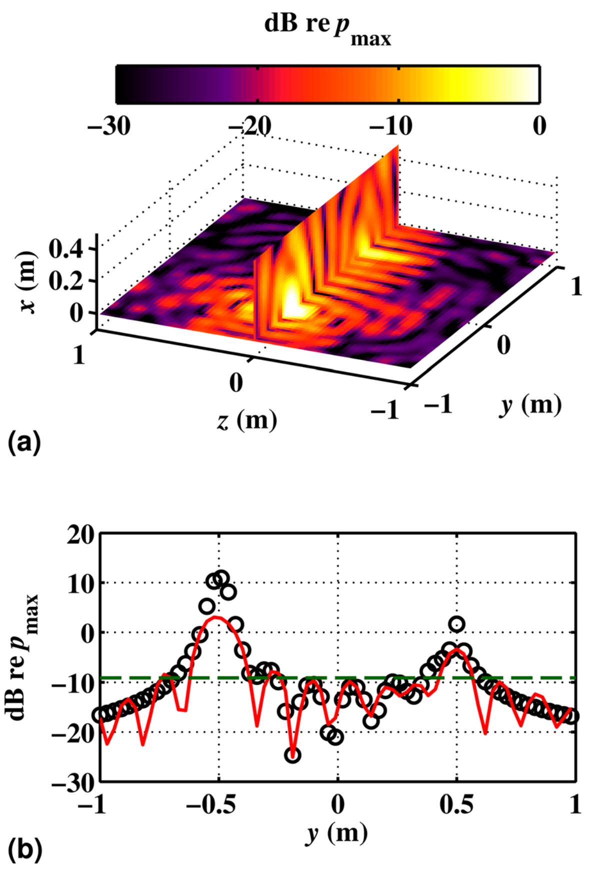

FIG. 5. (Color online) (a) Reconstructed SPLs at Γ_1 and Γ_2 after implementation of planar SONAH. (b) A comparison of select planar SONAH reconstructed SPLs (solid line) and benchmark SPLs (circles) within Γ_1, over reconstruction line 1 (at $z = 0$ m, $x = -0.001$ m). The dashed line marks the level that is 20 dB below the maximum benchmark level along line 1.

marks the level that is 20 dB below the maximum benchmark level. Reconstructed levels closely track benchmark levels, with less than 1 dB of error in the top 20 dB regions, except at $y = 0.5$ m (near the monopole singularities), and near $y = -0.5$ m (where the discontinuity between the vibrating piston and rigid sphere occurs). Errors near the piston are mitigated by an increase in SNR.

Planar SONAH reconstructions at Γ_1, Γ_2, and line 1 are given in Fig. 5. Note the presence of ripples in the three-dimensional field reconstruction of Fig. 5(a), which are a result of too much energy being parsed into the higher order (high wave number) functions. These ripples are shown to closely match the alternating peaks and nulls in the two-source interference pattern of the benchmark between $y = -0.5$ and 0.5 m [Fig. 5(b)], but they also extend outside this region where the interference does not actually generate ripples. In addition, the levels at two peak locations of $y = -0.5$ and 0.5 m are underestimated by the planar SONAH reconstruction by about 5 to 10 dB, due to the *lack* of energy in the higher order functions. Thus, the solution provided by the least-norm optimization resulted in a balanced solution that provided insufficient high wave number energy for some features of the field, and extraneous high wave number energy for other features. In contrast, the EWM used in the M-SONAH method provided a sufficient wave function set to avoid this problem.

The way to obtain a higher accuracy with the planar SONAH method in this case is to increase the sampling density of the hologram, thereby increasing the number and order of wave functions that can be included in the plane wave EWM. Higher sampling has a much greater effect on accuracy than the retraction distance (distance between actual source location and Γ_1), shape of the wave-function filter function, $F(k_x)$, or the removal of the simulated measurement noise from the hologram. Higher sampling can often be easily achieved in laboratory settings with computer-aided scanning systems where the current method may not be needed. However, the M-SONAH approach reduces the required number of measurements, which is desirable when measurement resources are limited and sparse sampling is necessary.

Another reason for the success of the M-SONAH method in this case is the effect that low-order modeling has on regularization. When high-order functions are used in an EWM, regularization can be particularly problematic for nonconformal measurement and wave function geometries. This is because evanescent waves decay at different rates for different wave functions, and the amplitude of evanescent radiation can vary across the measurement array, making the selection of a regularization filter shape tenuous. However, noise contamination has less effect on lower-order functions, so if a lower-order EWM can be found to represent a

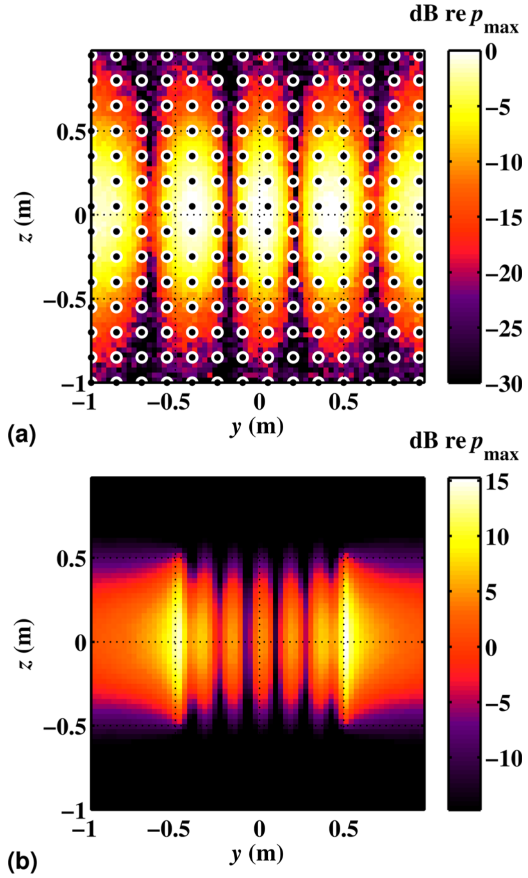

FIG. 6. (Color online) (a) Simulated SPLs at Ω_2. The dots show the locations of the hologram data that were used in NAH reconstructions. (b) Simulated SPLs at Γ_3 (benchmark).

complicated source more of the noise is filtered out and the regularization becomes more robust. Recall that some low-order sound field reconstructions have been performed without the need for regularization at all (Huang, 1990; Semenova and Wu, 2005).

B. Two line arrays

For the two-line-array simulation, SPLs at Ω_2 are shown in Fig. 6(a). A 30 dB SNR was again simulated in the hologram. Similar to the previous experiment, the benchmark at Γ_3 is provided in Fig. 6(b), and the M-SONAH reconstruction at Γ_3 is given in Fig. 7. Note that the reconstructed field is visually similar to the benchmark of Fig. 6(b). The reconstructed levels directly along one of the virtual source arrays, at $y = 0.5$ m (line 3 of Fig. 2), are plotted as the solid curve in Fig. 8(a). (Due to symmetry, the reconstruction and benchmark distributions are nearly identical near the second virtual source array at $y = -0.5$ m.) Finally, the reconstructed and benchmark levels running perpendicular to the extent of the sources, at $z = 0$ m (line 2 of Fig. 2) are shown in Fig. 8(b). In Fig. 8, all the M-SONAH reconstructions above the 20-dB-down mark are within a fraction of 1 dB of the benchmark. All important features of the simulated field, including source locations, levels, and interference patterns, are represented in the reconstructions.

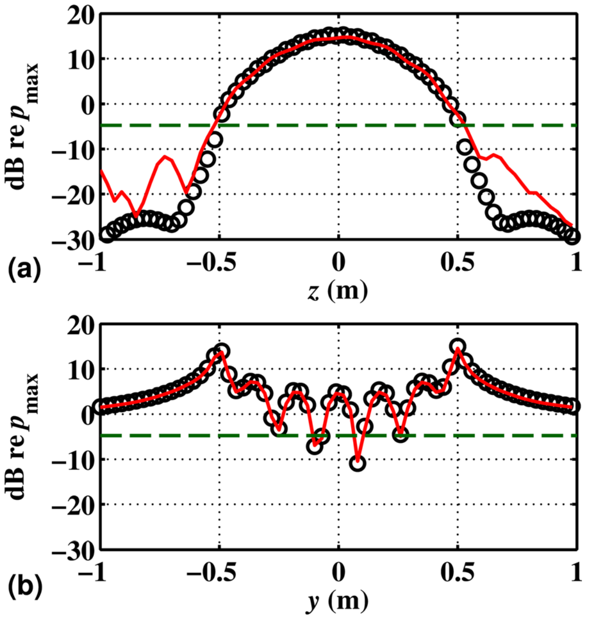

FIG. 8. (Color online) A comparison of select M-SONAH reconstructed SPLs (solid lines) and benchmark SPLs (circles) within Γ_3 ($x = -0.01$ m), (a) over reconstruction line 3 (at $y = 0.5$ m), and (b) over reconstruction line 2 (at $z = 0$ m). The dashed line marks the level that is 20 dB below the maximum benchmark level.

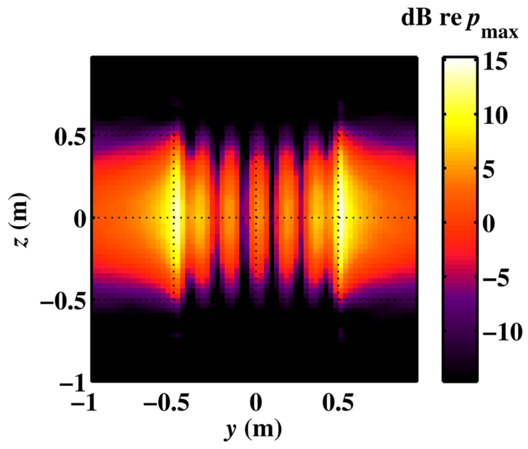

FIG. 7. (Color online) Reconstructed SPLs at Γ_3, calculated with M-SONAH.

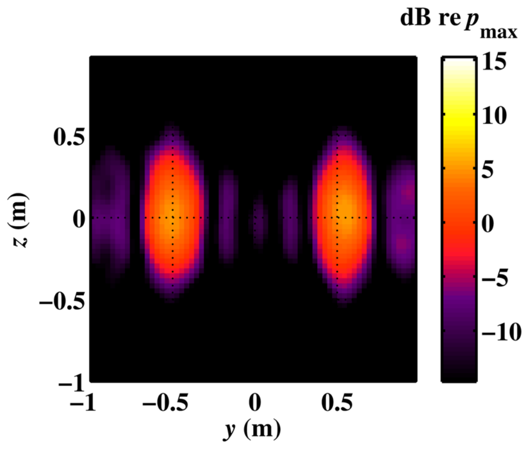

FIG. 9. (Color online) Reconstructed SPLs at Γ_3, calculated with planar SONAH.

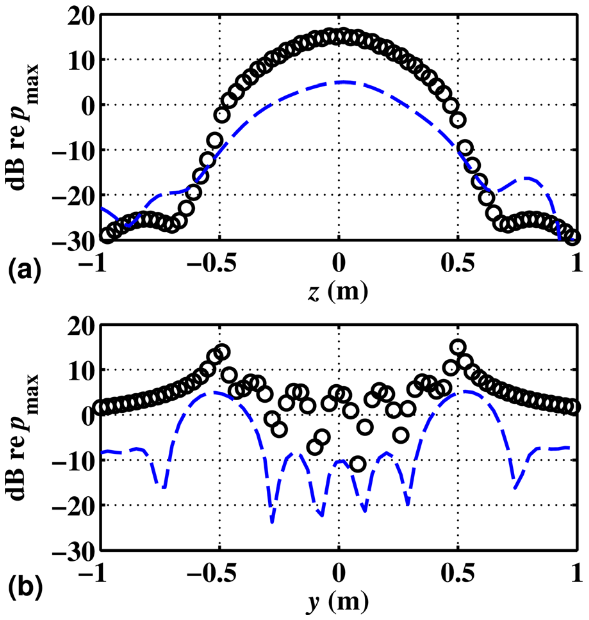

FIG. 10. (Color online) A comparison of select planar SONAH reconstructed SPLs (dashed lines) and benchmark SPLs (circles) within Γ_3 ($x = -0.01\,\text{m}$), (a) over reconstruction line 3 (at $y = 0.5\,\text{m}$), and (b) over reconstruction line 2 (at $z = 0\,\text{m}$).

Results for the planar SONAH reconstruction are provided in Figs. 9 and 10. Reconstructed SPLs at Γ_3 are shown in Fig. 9. A comparison of Fig. 9 to the simulated benchmark of Fig. 6(b) illustrates that the approximate source regions are localized within about a wavelength. In fact, careful inspection of Fig. 10(b), which displays the reconstructed levels at line 2, shows that planar SONAH is able to accurately localize the sources and the main features of the interference pattern, as the locations of the reconstructed peaks and nulls correspond to those of the benchmark. However, the SPLs at these locations are underestimated, typically by 10–15 dB. The levels along the extent of each source, as shown in Fig. 10(a), demonstrate that the source distributions are accurately represented, but are underestimated consistently by about 10 dB. This is because the plane wave EWM of measurements taken outside of the acoustic near field do not accurately represent the geometrical spreading that occurs with increasing distance from the sources. By employing cylindrical wave functions, M-SONAH is able to capture the geometrical spreading.

Figures 11 and 12 contain the reconstructions at Γ_3 from the cylindrical SONAH method. Figure 11, which shows the SPLs over the surface Γ_3, and Fig. 12(c), which shows SPLs along line 2, both show distinct maxima at $y = 0.5\,\text{m}$. This demonstrates how cylindrical SONAH can provide an accurate location for the first source, which is collocated with the center of the cylindrical wave functions used in the EWM. However, the second source at $y = -0.5\,\text{m}$ is missed [see Fig. 12(b)], because the limited set of basis functions does not represent it sufficiently. Theoretically, it should be possible to represent the secondary source with the inclusion of many higher-order terms in the EWM in order to approximate completeness. However, a denser measurement than the hologram used here would be required to capture these higher wave numbers. The ripples visible in the reconstructions of Figs. 11 and 12 are due to the parsing of significant energy into the higher orders of the axial components of the wave functions.

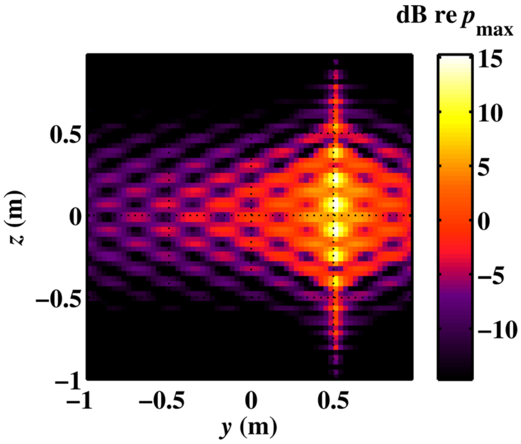

FIG. 11. (Color online) Reconstructed SPLs at Γ_3, calculated with cylindrical SONAH.

It is important to remember that no optimization of the hologram array or selection of wave function bases was

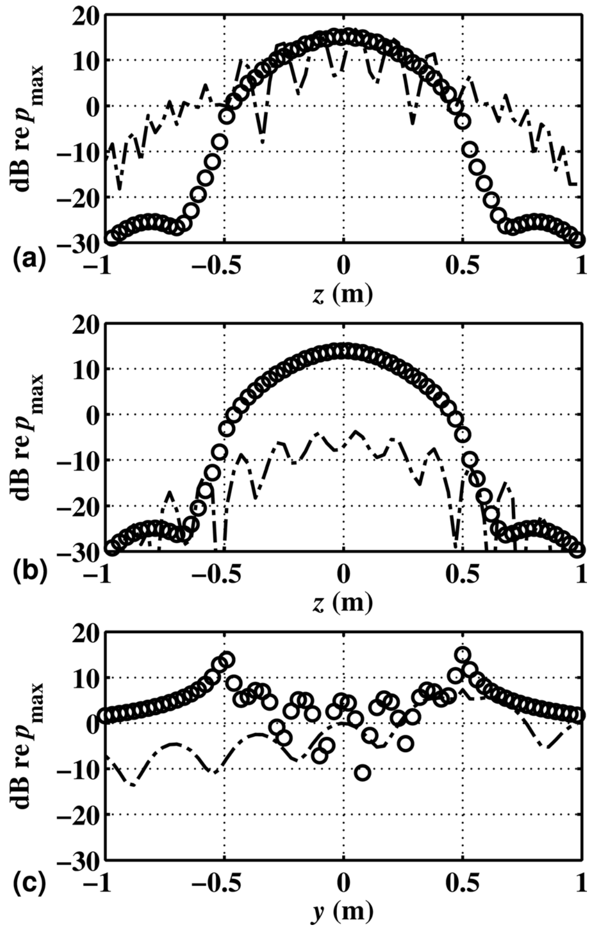

FIG. 12. A comparison of select cylindrical SONAH reconstructed SPLs (dashed-dotted lines) and benchmark SPLs (circles) within Γ_3 ($x = -0.01\,\text{m}$), (a) over reconstruction line 3 (at $y = 0.5\,\text{m}$), (b) over reconstruction line 4 (at $y = -0.5\,\text{m}$), and (c) over reconstruction line 2 (at $z = 0\,\text{m}$).

performed in these simulations. It is possible for planar and cylindrical SONAH methods to perform more successfully by altering the numerical measurement parameters, such as the distance between the hologram and sources, hologram density, or the inclusion of more wave functions. However, M-SONAH is robust under the hologram and EWM configurations employed in the current simulations, while the other methods are not.

V. CONCLUDING DISCUSSION

The selection of the equivalent wave model (EWM) in near-field acoustical holography (NAH) applications affects the accuracy of a reconstruction. In any inverse method, it is difficult to predict an "ideal" EWM expansion or array deployment for an arbitrary source, but a basis of wave functions that conform to the source shapes and locations requires fewer terms for an accurate reconstruction than a basis that does not reflect these source properties. A method for optimizing the number of expansion terms in an EWM was demonstrated by Wu (2000).

In this paper, a modified approach to the statistically optimized near-field acoustical holography algorithm (SONAH) has been presented, which facilitates the robust imaging of multisource fields by implementation of a user-defined EWM that leverages knowledge of source locations and shapes. This approach is called multisource SONAH, or M-SONAH. Numerical experiments were performed to demonstrate the accuracy of reconstruction that can be obtained for multisource configurations by using an intuitive EWM selection and M-SONAH in place of a strictly orthogonal EWM with a single wave function type and origin. In general, M-SONAH could be used in NAH applications where the sound field is generated by multiple sources of interest, where an additional noise source of known location and shape interferes with the source of interest, or even where scattering off an object alters the sound field. Preliminary applications of M-SONAH to reconstruct the sound field of a high-performance military jet in the presence of a large reflecting surface have been reported by Wall (2013) and Wall *et al.* (2013a, 2013b), and more detailed investigations are underway.

ACKNOWLEDGMENTS

The authors would like to thank Michael B. Muhlestein for his insightful contributions. A.T.W. was funded in part by an appointment to the Student Research Participation Program at U.S. Air Force Research Laboratory, Human Effectiveness Directorate, Warfighter Interface Division, Battlespace Acoustics administered by the Oak Ridge Institute for Science and Education through an interagency agreement between the U.S. Department of Energy and USAFRL.

Antoni, J. (**2012**). "A Bayesian approach to sound-source reconstruction: Optimal basis, regularization, and focusing," J. Acoust. Soc. Am. **131**(4), 2873–2890.

Bai, M. R. (**1992**). "Application of BEM (boundary element method)-based acoustic holography to radiation analysis of sound sources with arbitrarily shaped geometries," J. Acoust. Soc. Am. **92**(1), 533–549.

Cho, Y. T., Bolton, J. S., and Hald, J. (**2005**). "Source visualization by using statistically optimized near-field acoustical holography in cylindrical coordinates," J. Acoust. Soc. Am. **118**, 2355–2364.

Fahy, F., and Gardonio, P. (**2007a**). *Sound and Structural Vibration: Radiation, Transmission and Response* (Academic Press in an imprint of Elsevier, Oxford, UK), pp. 503–515.

Fahy, F., and Gardonio, P. (**2007b**). *Sound and Structural Vibration: Radiation, Transmission and Response* (Academic Press in an imprint of Elsevier, Oxford, UK), pp. 227–240.

Gomes, J., Jacobsen, F., and Bach-Andersen, M. (**2007**). "Statistically optimized near field acoustic holography and the Helmholtz equation least squares method: A comparison," in *Proceedings of the 8th International Conference on Theoretical and Computational Acoustics*, July 2–5, 2007, Heraklion, Greece.

Hald, J. (**1989**). "STSF—A unique technique for scan-based Near-field Acoustic Holography without restrictions on coherence," Technical Report No. 1, from Bruel & Kjaer, Naerum, Denmark.

Hald, J. (**2005**). "An integrated NAH/beamforming solution for efficient broad-band noise source location," SAE Technical paper 2005-01-2537.

Hald, J. (**2006**). "Patch holography in cabin environments using a two-layer handheld array with an extended SONAH algorithm," in *Proceedings of EuroNoise 2006*, Tampere, Finland.

Hald, J. (**2009**). "Basic theory and properties of statistically optimized near-field acoustical holography," J. Acoust. Soc. Am. **125**, 2105–2120.

Hald, J. (**2014**). "Scaling of plane-wave functions in statistically optimized near-field acoustic holography," J. Acoust. Soc. Am. **136**(5), 2687–2696.

Hart, D. M., Neilsen, T. B., Gee, K. L., and James, M. M. (**2013**). "A Bayesian based equivalent sound source model for a military jet aircraft," Proc. Mtg. Acoust. **19**, 055094.

Huang, Y. (**1990**). "Computer techniques for three-dimensional source radiation," Ph.D. dissertation, Pennsylvania State University.

Jacobsen, F., Chen, X., and Jaud, V. (**2008**). "A comparison of statistically optimized near field acoustic holography using single layer pressure-velocity measurements and using double layer pressure measurements (L)," J. Acoust. Soc. Am. **123**(4), 1842–1845.

Koopmann, G. H., and Benner, H. (**1982**). "Method for computing the sound power of machines based on the Helmholtz integral," J. Acoust. Soc. Am. **71**, 78–89.

Koopmann, G. H., Song, L., and Fahnline, J. B. (**1989**). "A method for computing acoustic fields based on the principle of wave superposition," J. Acoust. Soc. Am. **86**, 2433–2438.

Lee, M., and Bolton, J. S. (**2006**). "Scan-based near-field acoustical holography and partial field decomposition in the presence of noise and source level variation," J. Acoust. Soc. Am. **119**(1), 382–393.

Maynard, J. D., Williams, E. G., and Lee, Y. (**1985**). "Near field acoustic holography: 1. Theory of generalized holography and the development of NAH," J. Acoust. Soc. Am. **78**, 1395–1413.

Mollo-Christensen, E. (**1967**). "Jet noise and shear flow instability seen from an experimenter's viewpoint," J. Appl. Mech. **34**, 1–7.

Moon, T. K., and Stirling, W. C. (**2000**). *Mathematical Methods and Algorithms for Signal Processing* (Prentice Hall, New York), pp. 139 and 183.

Morgan, J., Gee, K. L., Neilsen, T. B., and Wall, A. T. (**2012**). "Simple-source model of military jet aircraft noise," Noise Control Eng. J. **60**, 435–449.

Morse, P. M., and Ingard, K. U. (**1968**). *Theoretical Acoustics* (Princeton University Press, Princeton, NJ), pp. 332–346.

Rayess, N., and Wu, S. F. (**2000**). "Experimental validations of the HELS method for reconstructing acoustic radiation from a complex vibrating structure," J. Acoust. Soc. Am. **107**, 2955–2964.

Sarkissian, A. (**2005**). "Method of superposition applied to patch near-field acoustic holography," J. Acoust. Soc. Am. **118**(2), 671–678.

Semenova, T., and Wu, S. F. (**2005**). "On the choice of expansion functions in the Helmholtz equation least-squares method," J. Acoust. Soc. Am. **117**, 701–710.

Shah, P. N., Vold, H., and Yang, M. (**2011**). "Reconstruction of far-field noise using multireference acoustical holography measurements of high-speed jets," AIAA Paper 2011-2772, Portland, OR.

Steiner, R., and Hald, J. (**2001**). "Near-field acoustical holography without the errors and limitations caused by the use of spatial DFT," Int. J. Sound Vib. **6**, 83–89.

Tam, C. K. W., Viswanathan, K., Pastouchenko, N. N., and Tam, B. (**2010**). "Continuation of the near acoustic field of a jet to the far field. Part II:

Experimental validation and noise source characteristics," AIAA Paper 2010-3729, Stockholm, Sweden.

Tamura, M. (**1990**). "Spatial Fourier transform method of measuring reflection coefficients at oblique incidence. I: Theory and numerical examples," J. Acoust. Soc. Am. **88**, 2259–2264.

Van Veen, B. D., and Buckley, K. M. (**1988**). "Beamforming: A versatile approach to spatial filtering," IEEE ASSP Magazine, pp. 4–24.

Veronesi, W. A., and Maynard, J. D. (**1989**). "Digital holographic reconstruction of sources with arbitrarily shaped surfaces," J. Acoust. Soc. Am. **85**, 588–598.

Wall A. T. (**2013**). "The characterization of military aircraft jet noise using near-field acoustical holography methods," Ph.D. dissertation, Brigham Young University.

Wall, A. T., Gee, K. L., and Neilsen, T. B. (**2013a**). "Modified statistically optimized near-field acoustical holography for jet noise characterization," Proc. Mtg. Acoust. **19**, 055013.

Wall, A. T., Gee, K. L., Neilsen, T. B., and James, M. M. (**2013b**). "Acoustical holography imaging of full-scale jet noise fields," in *Proceedings of Noise-Con 2013*.

Wall, A. T., Gee, K. L., Neilsen, T. B., Krueger, D. W., James, M. M., Sommerfeldt, S. D., and Blotter, J. D. (**2012**). "Full-scale jet noise characterization using scan-based acoustical holography," AIAA Paper 2012-2081, Colorado Springs, CO.

Wang, Z., and Wu, S. F. (**1997**). "Helmholtz equation–least-squares method for reconstructing the acoustic pressure field," J. Acoust. Soc. Am. **102**, 2020–2032.

Weinrich, G., and Arnold, E. B. (**1980**). "Method for measuring acoustic radiation fields," J. Acoust. Soc. Am. **68**(2), 404–411.

Williams, E. G. (**1999**). *Fourier Acoustics: Sound Radiation and Nearfield Acoustical Holography* (Academic Press, San Diego, CA), pp. 149–182.

Williams, E. G. (**2001**). "Regularization methods for near-field acoustical holography," J. Acoust. Soc. Am. **110**, 1976–1988.

Williams, E. G. (**2003**). "Continuation of acoustic near-fields," J. Acoust. Soc. Am. **113**, 1273–1281.

Wu, S. F. (**2000**). "On reconstruction of acoustic pressure fields using the Helmholtz equation least squares method," J. Acoust. Soc. Am. **107**, 2511–2522.